Journal of Power Sources 405 (2018) 80–88

Contents lists available at ScienceDirect

Journal of Power Sources

journal homepage: www.elsevier.com/locate/jpowsour

A green and template-free synthesis process of superior carbon material with ellipsoidal structure as enhanced material for supercapacitors

Yanzhi Sun[a], Shicheng Guo[a], Wei Li[b], Junqing Pan[a,*], Carlos Fernandez[c], Raja Arumugam Senthil[a], Xueliang Sun[d,**]

[a] State Key Laboratory of Chemical Resource Engineering, Beijing Engineering Center for Hierarchical Catalysts, Beijing Advanced Innovation Center for Soft Matter Science and Engineering, Beijing University of Chemical Technology, Beijing 100029, China
[b] Department of Engineering Technology and Texas Center for Superconductivity, University of Houston, Houston, TX, 77204, USA
[c] School of Pharmacy and Life Sciences, Robert Gordon University, Aberdeen, AB10 7GJ, UK
[d] Department of Mechanical and Materials Engineering, University of Western Ontario, London, ON, N6A 5B9, Canada

HIGHLIGHTS

- The ellipsoid-like porous carbon material is prepared with a template-free method.
- The raw material $Al(OH)_3$ can be recovered from a hydrolysis process of Bayer method.
- The obtained carbon material shows excellent electrochemical performance.

GRAPHICAL ABSTRACT

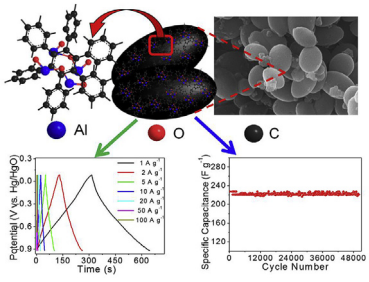

ARTICLE INFO

Keywords:
3D materials
Porous carbon
Supercapacitor
Template free
Metal organic frameworks

ABSTRACT

Metal Organic Frameworks or related carbon materials are the ideal materials for supercapacitors due to their high surface area and unique porous structure. Here, we propose a new green and recyclable synthesis method of porous carbon. Aluminum hydroxide ($Al(OH)_3$) and trimesic acid (BTC) are employed as raw materials to obtain aluminium trimesic (denoted as Al-BTC) via their covalent reaction. Then, the porous carbon is obtained through carbonization and dissolving process to remove the aluminum oxide (Al_2O_3). $Al(OH)_3$ is recovered by the Bayer method for the next batch. The SEM images show that the porous carbon has rugby-like morphology with the same of 400 nm wide and 1000 nm long which indicates the porous carbon with c/a ratio of 2.5 providing the largest specific volume surface area. The sample offers 306.4 F g^{-1} at 1 A g^{-1}, and it can retain 72.2% even at the current density of 50 A g^{-1}. In addition, the porous carbon provides excellent durability of 50,000 cycles at 50 A g^{-1} with only 5.05% decline of capacitance. Moreover, the porous carbon has an ultrafast charge acceptance, and only 4.4 s is required for one single process, which is promising for application in electric vehicles.

1. Introduction

In order to meet the growing energy demand, a great number of research has focused on developing new energy materials with long cycling life for the application in supercapacitors (SPs) [1–6]. SPs or electrochemical capacitors with ultrahigh power density and good

* Corresponding author.
** Corresponding author.
E-mail addresses: jqpan@mail.buct.edu.cn (J. Pan), xsun9@uwo.ca (X. Sun).

https://doi.org/10.1016/j.jpowsour.2018.10.034
Received 15 July 2018; Received in revised form 21 September 2018; Accepted 9 October 2018
0378-7753/

durability are widely used in hybrid electric vehicles (HEV), military space, and biomedical equipment, becoming one of the most important energy-storage devices [7–12]. SPs usually used the porous carbon (PC) [13], activated carbon [9], graphene [14–16], and carbon nanotubes [17,18] as active materials because of their high chemical stability, large surface area, and special nano effects [19].

In recent years, carbon materials with 2D structure, such as graphene with large surface area, high conductivity, and short ion diffusion distance, have gradually attracted researchers' attention [20]. The most effective preparation method for these materials is using graphene oxide to prepare 2D interconnected carbon nanosheets with a Brunauer-Emmett-Teller (BET) surface area in the range of 1400–2200 $m^2 g^{-1}$ [21]. However, the 2D carbon nanosheets may easily overlap with each other in the practical electrodes, which drastically reduce the surface area and the electrochemical performance [22]. To resolve the overlap problem and further enable the SPs to have higher energy densities, various materials with new synthesis methods have been proposed [23–30]. However, the dense structure and amorphous morphology limit their energy density, power density and durability.

More recently, metal-organic frameworks (MOFs) have attracted much interests as novel types of nanoporous crystalline materials owing to their large surface area, high pore volume and tunable morphology with 3D structure [31–34]. MOFs have been fabricated through metal-containing nodes in connection with organic ligands and also utilized as active materials in different applications, such as gas separation, gas and vapor storage, water purification, energy storage device, etc [35,36]. In recent years, the 3D structured PC materials derived from MOF precursor via thermal carbonization in inert atmosphere with large surface area and high porosity have been reported for the application in SPs. For example, Zhang et al. [37] prepared PC from Ni-based MOF with specific surface area of 1143 $m^2 g^{-1}$ and achieved a specific capacitance of 211 $F g^{-1}$ at a current density of 1 $A g^{-1}$. Liu et al. [38] developed PC nanosheets using Al-based MOF with a specific capacitance of 88 $F g^{-1}$ at a current density of 1 $A g^{-1}$ in 6 M KOH electrolyte. Yang et al. [39] derived the PC with large surface area of 2816 $m^2 g^{-1}$ and high porosity from Zn-based MOF for SPs and obtained a specific capacitance of 170 $F g^{-1}$ at current density of 1 $A g^{-1}$. Xin et al. [33] also synthesized N-doped PC/graphene composite from hierarchical Zn-based MOF for SPs, supplying a high specific capacitance of 245 $F g^{-1}$ at a current density of 1 $A g^{-1}$. Yan et al. [34] reported PC from Al-based MOF for SPs, which showed a specific capacitance of 232.8 and 173.6 $F g^{-1}$ at current density of 0.1 and 1 $A g^{-1}$ respectively. In addition, Zhang et al. [40] prepared the hierarchical PC from Al-based MOF for SPs, which shows a high specific capacitance of 249 $F g^{-1}$ at a current density of 1 $A g^{-1}$.

The above reports reveal that the surface morphology and pore volume of the carbon materials have significant impact on the electrochemical performance of SPs. Moreover, the combination of mesopores and micropores of PC can enhance the capacitance as the electrolyte solution moves via the mesopores and also electrolyte ions are stored in the micropores during the charging/discharging process [37–41]. However, it is found that their uniform 3D morphology is dependent on the addition of template, and their electrochemical performance is dependent on the contained metal ions and the subsequent high temperature carbonization process. These three problems greatly increased the cost of the materials and limited the large-scale application. In addition, recycling of involved chemicals as the next batch's raw materials and designing a metal free materials to decrease the pollution of waste chemicals have never been reported so far.

Herein, we propose a facile, green and template-free method to prepare PC by the carbonization of rugby-like Al-based MOF, (Al-BTC, $(Al_{12}O(OH)_{18}(H_2O)_3(Al_{12}(OH)_4)(BTC)_6 \cdot 24H_2O)$), in which $Al(OH)_3$ and BTC along with CTAB as an additive are employed as raw materials to prepare hierarchical nano PC. In addition, our proposed methodology presents the advantage of recycling of $Al(OH)_3$ which is recovered through the hydrolysis process by Bayer method and used as raw material for the next batch. The obtained PC has a high specific surface area of 1400 $m^2 g^{-1}$ containing both micropores (< 2 nm) and mesopores (2–5 nm). The obtained PC sample offers a superior electrochemical performance for SPs with high specific capacitance of 306.4 $F g^{-1}$ at current density of 1 $A g^{-1}$, excellent durability of 50,000 cycles at ultrahigh current density of 50 $A g^{-1}$ with only 5.05% decay, and remarkable ultrafast charge acceptance of 4.4 s for one charge process.

2. Experimental section

2.1. Preparation Al-MOFs and porous carbon

1.651 g aluminum hydroxide (65%, Tianjin Zhiyuan Chemical Reagent Co., Ltd.) mixed with 5 drops of 1 mol L^{-1} HNO_3 was dispersed in 30 ml deionized water, marked as solution A. 0.663 g trimesic acid (99%, Guangdong Wengjiang Reagent Co., Ltd.) and 1.812 g cetyltrimethylammonium bromide (CTAB) (99%, Tianjin Jingke Fine Chemical Research Institute) was dissolved in 30 ml ethanol, marked as solution B. Solution A and B were mixed in 100 ml three neck bottle under stirring for 30 min. Then, the mixture was moved to a 100 ml Teflon-lined stainless steel autoclave (100 ml, Zhengzhou Boke Co., Ltd., 304 stainless steel + PTFE) to be heated at 120 °C for 9 h. After finishing the reaction, the product was filtered and washed deionized water, and then, obtained Al-BTC was drying in a vacuum oven at 60 °C for 12 h. After that, 0.5 g Al-BTC was moved to a nickel boat and carbonized at 800 °C for 2 h in a vacuum tube furnace at a heating rate of 5 °C min^{-1}, followed by natural cooling to room temperature to obtain the C/Al_2O_3 composite. The C/Al_2O_3 was dissolved in 8 M NaOH-1.2 M $NaAl(OH)_4$ solution at 120 °C under stirring for 10 min to remove Al_2O_3. The product was filtered and washed with deionized water until the filtrate presented neutral to obtain porous carbon (PC).

2.2. Morphological and structural characterizations

The morphology and surface structure of synthesized Al-BTC, C/Al_2O_3 and PC samples were characterized by a scanning electron microscope equipped with energy dispersive spectroscopy (SEM/EDX, Zeiss SUPRA 55). The structure of the obtained samples were characterized by X-ray diffraction (XRD) on a Bruker D8 Advance X-Ray Diffractometer using a Cu Kα, and the scanning rate was 10° min^{-1} in the range of scanning angle (2 θ) from 5° to 90°. The high resoluation-transmission electron microscopy (HR-TEM) images of samples were collected on a Philips CM200FEG Field Emission Microscope. The Brunauer Emmett Teller (BET) specific surface area, pore volume and pore size distribution of the as-prepared samples were studied using nitrogen adsorption-desorption analysis by a QuandasorbSI model particle analyzer. Thermal gravimetric analysis (TGA) was performed on a NETZSCHSTA 4449F 3STA449F3A-024-M model thermal analyzer in the temperature range from 20 °C to 900 °C under N_2 atmosphere at a heating rate of 10 °C min^{-1}. The X-ray photoelectron spectra (XPS) were performed on a Thermo Fisher ESCALAB 250 X-ray photoelectron spectrometer with monochromated Al Kα radiation source.

2.3. Electrochemical tests

800 mg samples, 200 mg expanded graphite (99.9%, Qingdao Laixi Fine Graphite) and 50 mg PTFE (60 wt%, Guangzhou Songbai Chemicals) were mixed and ground in an agate mortar for 30 min. Then, the obtained paste was rolled into 50 μm thick as electrode film and cut into the size of 10 mm × 10 mm, and applied on the of nickel foam of the same size (density: 550 ± 30 g m^{-2}, pores per inch: 100 ± 30, thickness: 1.8 ± 0.1 mm, purchased from Changsha Liyuan New Materials) to form the composite plate, which was then pressed by a pressing machine (YP-15A, Shanghai Jingsheng Instrument) for 30 s at 10 MPa to obtain working electrode.

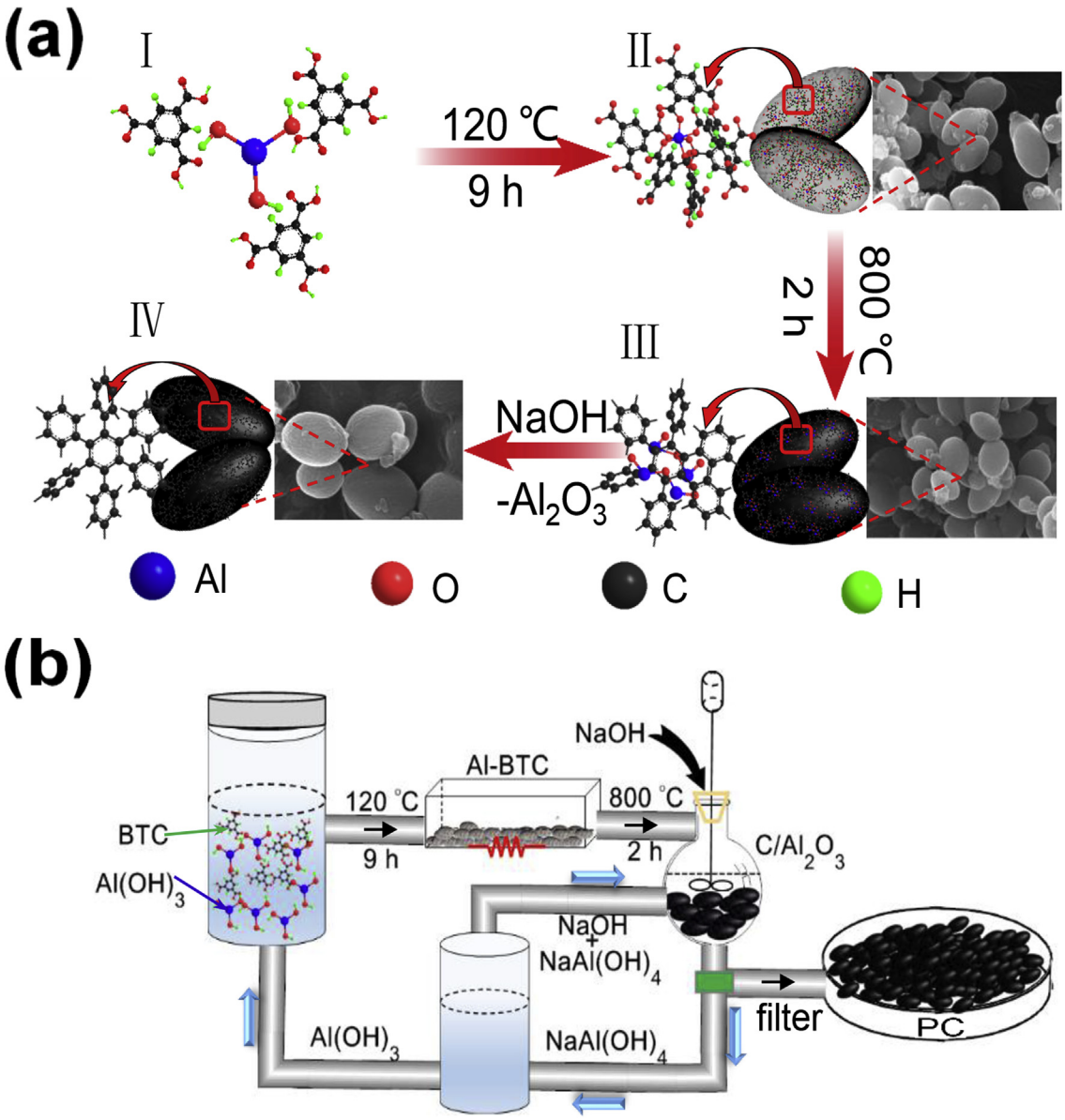

Fig. 1. (a) Diagram from rugby-like Al-BTC to rugby-like PC and (b) diagram of preparation route of PC.

Electrochemical tests were performed by a three electrodes system using 6 M KOH as electrolyte at room temperature. A 10 mm × 10 mm Nickel plate used as auxiliary electrode and a Hg/HgO electrode as reference electrode. The charge/discharge tests were carried out by a LAND CT2001A battery test system (Jinnuo Wuhan Corp, China) at room temperature. Cyclic voltammetry tests (CV, scan range: 0.9-0.1 V (Vs. Hg/HgO), scan rate: 1–50 mV s^{-1}) were performed on a CS300 cell test system (Wuhan CorrTest Instruments Co., Ltd.).

3. Results and discussion

Fig. 1a and b shows the schematic diagram of the process step by step from $Al(OH)_3$ and BTC to the final formation of Al-BTC, C/Al_2O_3, and PC. Fig. 1 aII illustrates that Al-BTC has its own specific structure of rugby-like particle, which depends on the spatial orientation of Al^{3+} and BTC. Fig. 1 aIII displays the C/Al_2O_3 composite obtained during the decarboxylation process at 800 °C. Fig. 1 aIV shows a PC after removing Al_2O_3. In the carbonization process of Al-BTC at high temperatures, CO_2 can easily escape from carboxyl functional groups and hence, the carbonized resultants have welldeveloped uniform holes. In addition, the resultant carbon material contains Al_2O_3 nanoparticles owing to the thermal stablility of Al_2O_3 materials. To obtain a larger PC surface area, NaOH−$NaAl(OH)_4$ was used to remove Al_2O_3 particles from obtained carbon material by Bayer process. $NaAl(OH)_4$ solution was obtained by a regeneration process of NaOH−$NaAl(OH)_4$ solution. Then, $Al(OH)_3$ can be recycled and used as a raw material for the next preparation of Al-BTC again, thus forming a green preparation process. Fig. 1b shows the green cycling synthesis of Al-BTC using Bayer process. Fig. S1, S2, and S3 illustrate the photographs, SEM images and XRD patterns, respectively, in which (a) $Al(OH)_3$ is the raw materials and (b) is the recovered $Al(OH)_3$ from Bayer process.

Fig. 2a, b and c show the SEM and element mapping images of the obtained Al-BTC, C/Al_2O_3 composite and PC, respectively. As seen from Fig. 2a, Al-BTC exhibits a typical rugby-like structure, with the average size of particles found to be circa 400 nm in width and 1000 nm in length. Fig. 2b displays that the morphology of C/Al_2O_3 composite retains uniform rugby-like surface, and the surface becomes slightly rough after the carbonation process. This could be attributed to the emission of gases like H_2O, CO or CO_2 during the thermal decomposition process. Fig. 2c shows the obtained PC by dissolving the Al_2O_3

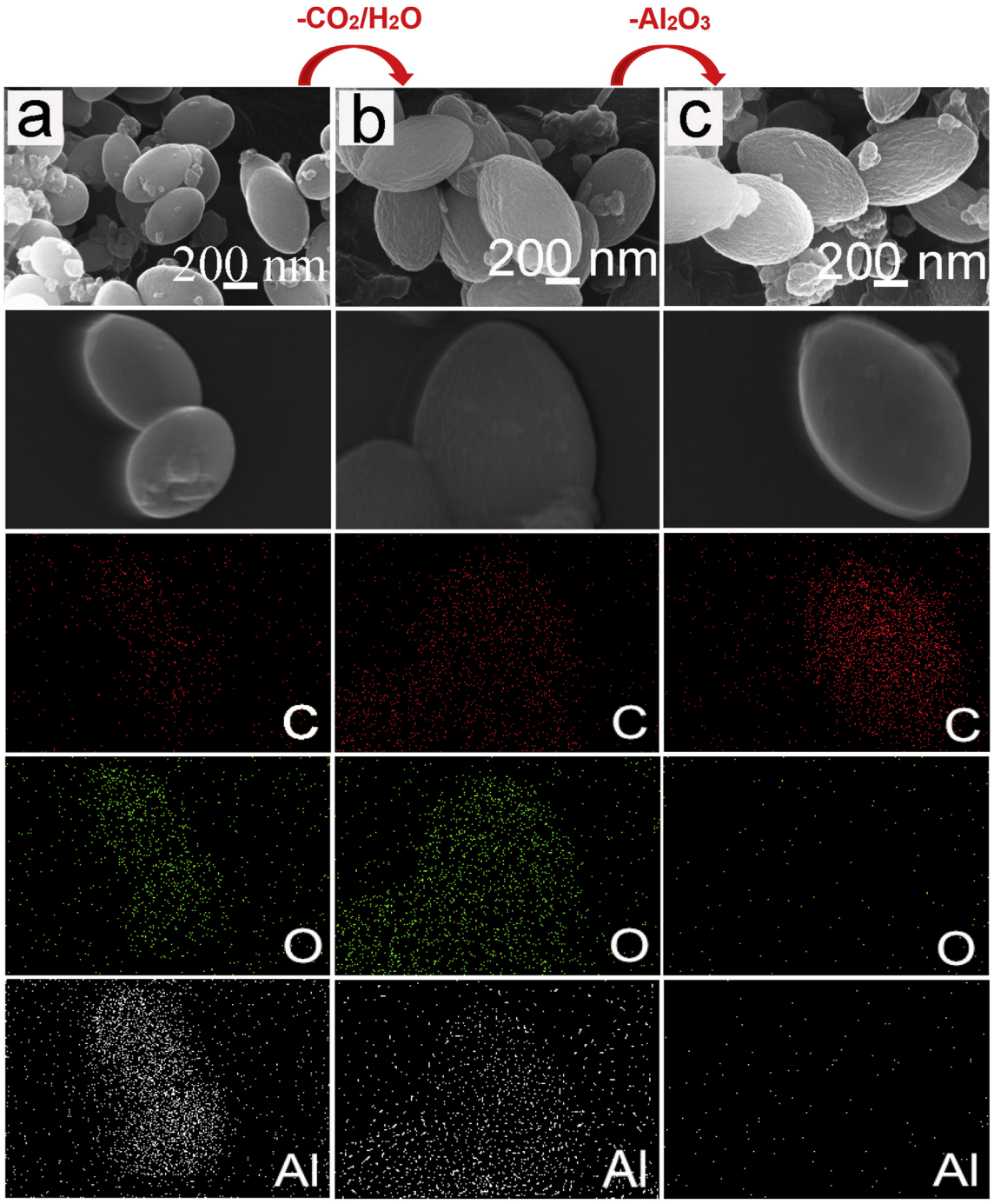

Fig. 2. SEM and mapping images of (a) Al-BTC synthesized at 120 °C for 9 h, (b) C/Al_2O_3 composite obtained by carbonizing Al-BTC under vacuum at 800 °C for 2 h and (c) PC obtained by dissolving sample b in NaOH− $NaAl(OH)_4$ solution under 120 °C and stirring for 10 min.

from C/Al_2O_3 composite into a NaOH−$NaAl(OH)_4$ solution by Bayer method. The PC still retains its rugby-like 3D structure, indicating that the morphology of the product is very stable in the alkaline media, even in concentrated NaOH solution. C, Al and O elements can be observed in Fig. 2a and b before NaOH treatment. However, after NaOH treatment shown in Fig. 2c, Al and O elements almost disappear, revealing the succesfull removal of Al_2O_3 by NaOH treatment.

Fig. S4 indicates the TGA curve of the obtained Al-BTC from 20 to 900 °C at heating rate of 10 °C min^{-1} in N_2 atmosphere. The results show that the Al-BTC begins to form the carbon skeleton and Al_2O_3 during the carbonization process from 500 to 900 °C. The mass loss in this process is circa 30% which is very close to the calculated value by the decomposition reaction from Al-BTC to C/Al_2O_3 composite. The photographs of the obtained Al-BTC, C/Al_2O_3 and PC are shown in Fig. S5. Fig. S6 and S7 show SEM images of Al-BTC samples obtained at different time and temperatures, respectively. Fig. S8 provides the charge and discharge curves of the obtained PC. The results show that the PC provides the highest electrochemical performance under the optimal preparation conditions of 120 °C for 9 h and carbonization conditions of 800 °C for 2 h, respectively.

Fig. 3a displays the XRD patterns of the obtained Al-BTC, C/Al_2O_3 composite and PC. The XRD pattern of Al-BTC basically conforms to those characteristic peaks of the Al-BTC reported in the literature [42]. The composite of C/Al_2O_3 sample exhibits two broad diffraction peaks at about $2\theta = 25°$ and 45°, which are related to (002) and (101) diffraction planes of porous carbon (JCPDS No. 41–1487), respectively.

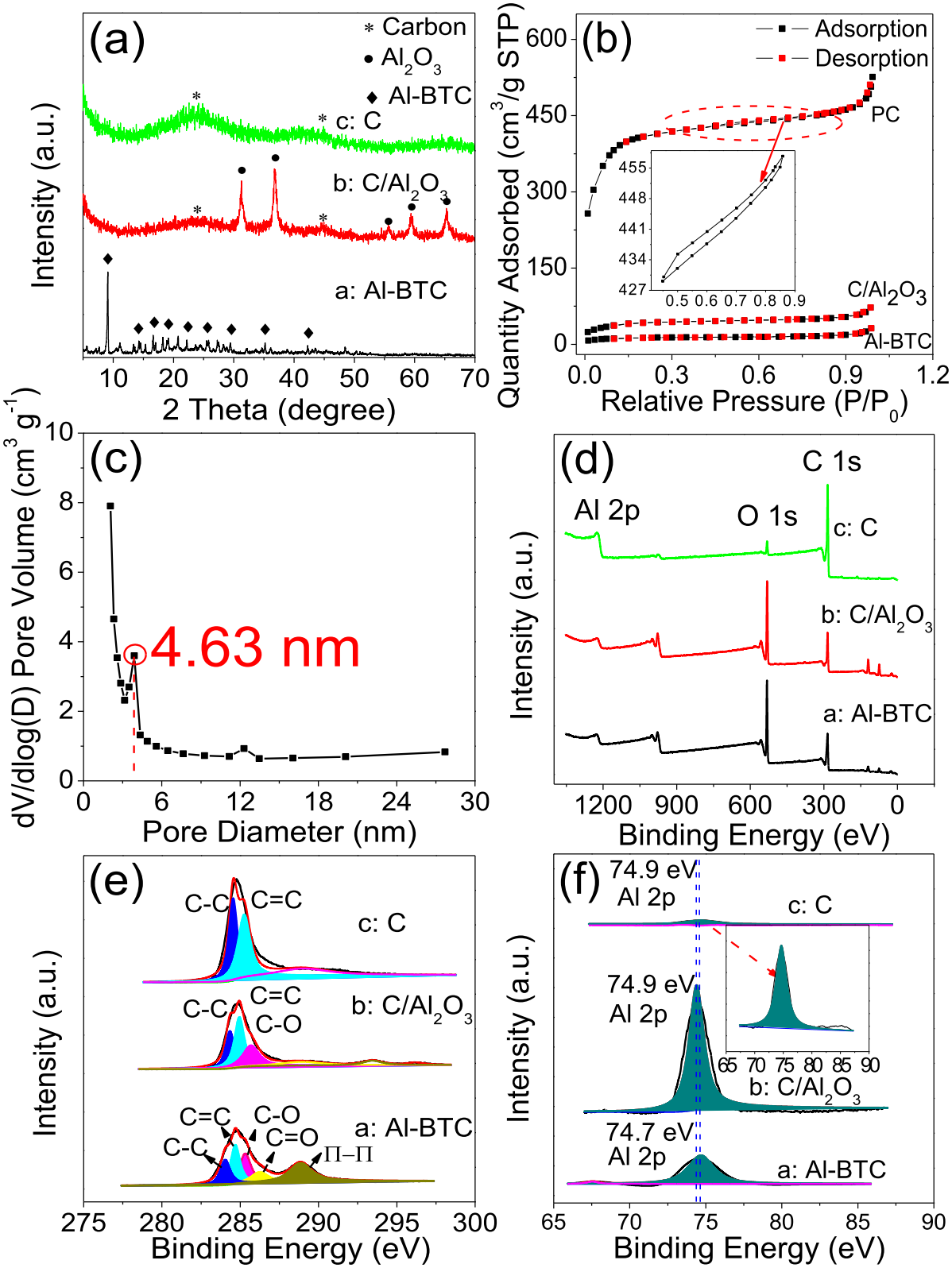

Fig. 3. (a) XRD patterns of Al-BTC, C/Al_2O_3 and PC, (b) N_2 adsorption-desorption isotherms curves, (c) pore size distribution of the obtained carbon and (d), (e) and (f) overview of XPS spectra, C 1s spectra and Al 2p spectra of Al-BTC, C/Al_2O_3 and PC, respectively.

And also several sharp diffraction peaks appear at 2θ = 31.83°, 37.55°, 56.72°, 60.49° and 66.46°, which can be indexed to (220), (311), (422), (511) and (440) diffraction planes of the Al_2O_3 (JCPDS No. 47–1292), respectively. These diffraction peaks are in good agreement with the earlier reports on Al_2O_3 [43] and carbon [44] in literature, indicating the composite contains the amorphous carbon and crystallized Al_2O_3. The PC exhibits only two broad diffraction peaks at about 2θ = 25° and 45°, indicating the successful removal of Al_2O_3 nanoparticles by Bayer process and the achievement of a high purity PC material. Fig. 3b shows the BET test results of Al-BTC, C/Al_2O_3 composite and PC. The specific

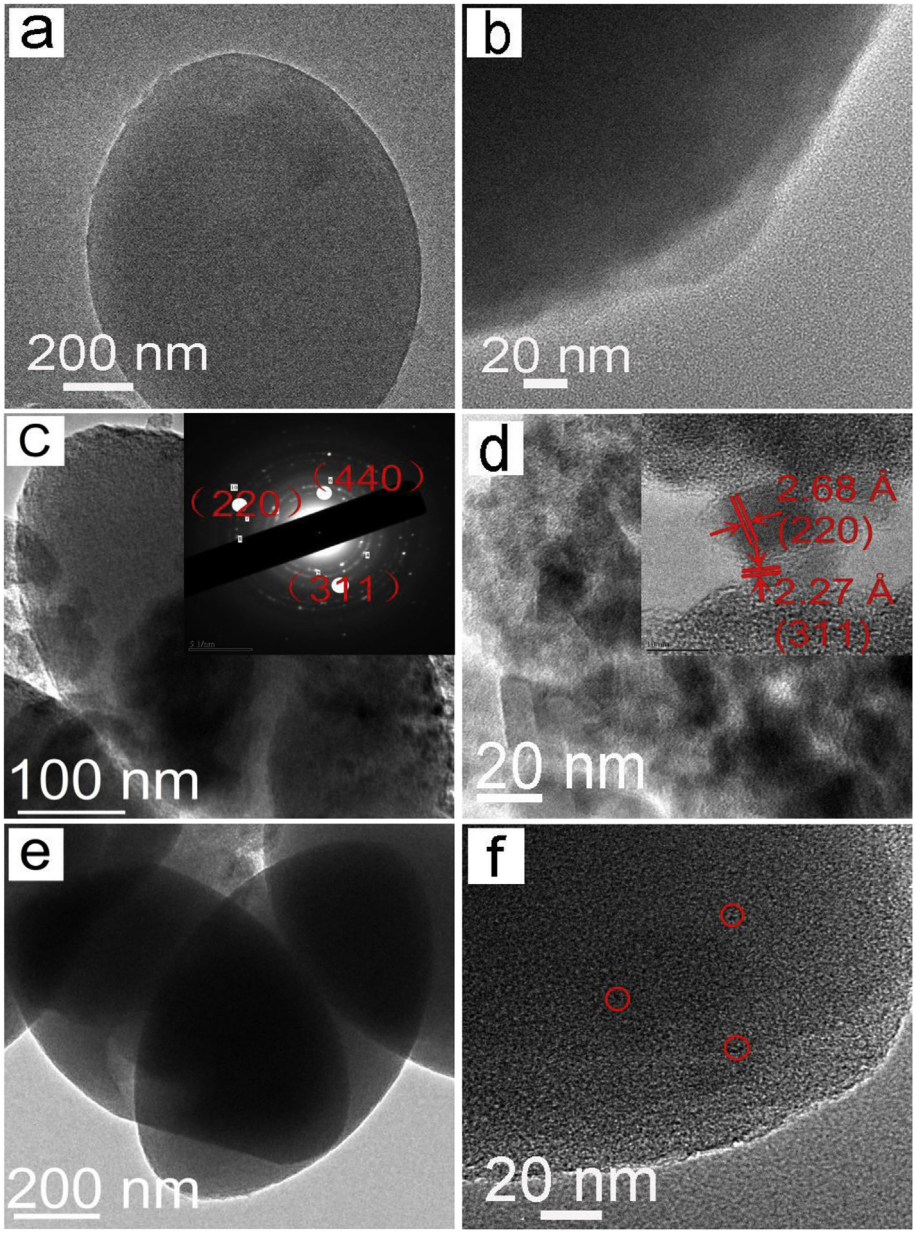

Fig. 4. Different magnification HR-TEM images of (a,b) Al-BTC, (c,d) C/Al_2O_3 and (e,f) PC.

surface areas of the three materials are found to be 45.2, 146.1 and 1400 $m^2 g^{-1}$, indicating that the process of decarboxylation and carbonization, especially the subsequent dissolution of Al_2O_3, can greatly improve the carbon surface area. In addition, the carboxyl groups and Al_2O_3 are the natural pore forming agents. Fig. 3d, e, and f show the overview XPS spectra of C 1s and Al 2p of Al-BTC, the composite of C/Al_2O_3 and the PC. As seen from Fig. 3d, the peak intensities of C, O, and Al decrease, which is well consistent with the previous element mapping and XRD results. Fig. 3e shows the detailed XPS spectra of C 1s after peak separation. The peaks of carbon element of Al-BTC at 284.2, 284.6, 285.3, 287.1 eV, correspond to the following bonds: C=C, C−C, C−O, and C=O, respectively. The peak situated at 290.6 eV is attributed to the π-π* electronic transitions. The peaks of carbon element of C/Al_2O_3 at 284.6 eV correspond to C 1s. Furthermore, the peaks of carbon located at 284.8 eV correspond to C 1s. Fig. 3f shows the detailed XPS spectra of Al 2p after peak separation. The peaks of aluminum found in the following compounds: Al-BTC, C/Al_2O_3 and C at 74.7, 74.9, 74.9 eV, correspond to Al 2p. The bonding of Al in Al-BTC belongs to the functional group −COO−Al, which is different to that in C/Al_2O_3. Therefore, the peaks of aluminum in Al-BTC is different to that of C/Al_2O_3. Moreover, the observed very low intensity of Al peaks in the PC sample indicates the trace Al_2O_3 in the obtained PC.

Fig. 4 illustrates the HR-TEM images of the obtained Al-BTC, C/Al_2O_3 and PC under different magnifications. The inserted image of Fig. 4c exhibits the SAED patterns of C/Al_2O_3, in which the diffraction rings clearly reflect the diffraction spots, corresponding to the crystals planes of (220), (311) and (440) of γ-Al_2O_3. The inserted HR-TEM image (Fig. 4d) displays legible lattices fringes in which the adjacent lattices are 0.268 nm and 0.220 nm, corresponding to the (220) and (311) planes of γ-Al_2O_3, respectively, which match the results from the XRD pattern. The nano particles size of γ-Al_2O_3 is 4.64 nm are very close to the size of the hole (4.63 nm) tested by BET. As observed from Fig. 4e and f, after adding concentrated NaOH (8 M) solution a significant number of holes appear due to removing the nano Al_2O_3 particles, leading to a considerable increase in surface area of the PC. The larger surface area is very beneficial to obtaining higher specific capacitance of the electrode material for SPs.

Fig. 5a illustrates GCD curves of PC under different current densities

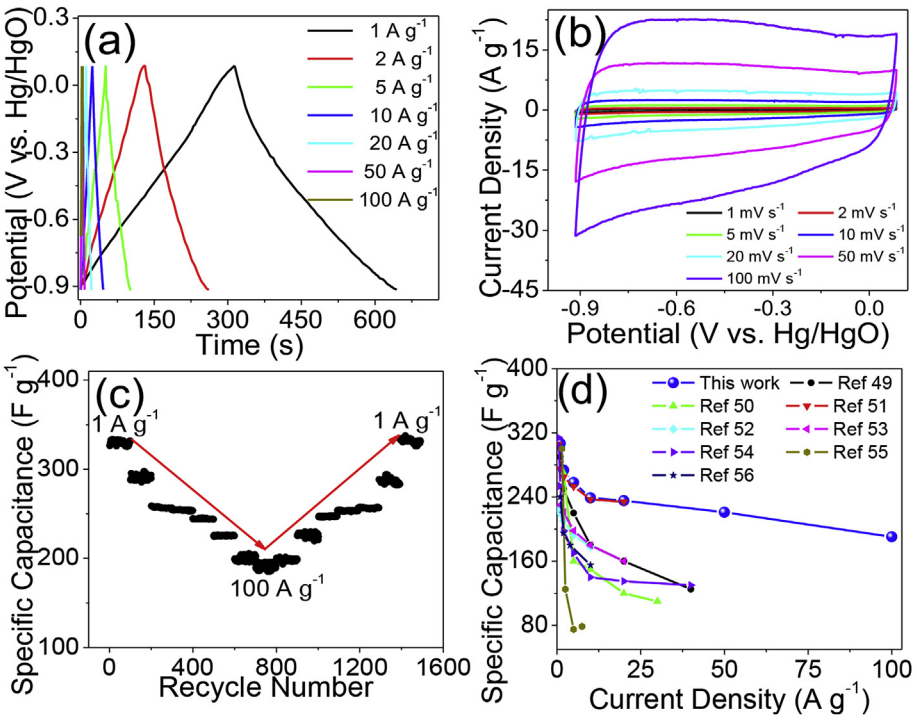

Fig. 5. (a) GCD curves of PC at different current densities from 1 to 100 A g^{-1} in 6 M KOH, (b) CV curves of the PC at different scan rates from 1 to 100 mV s^{-1} in the range from −0.9 to 0.1 V (vs. Hg/HgO) in 6 M KOH at 298 K, (c) SCs cycling properties of the PC at various current densities, and (d) SCs of the obtained carbon as compared with the other carbons reported in literature at different current densities.

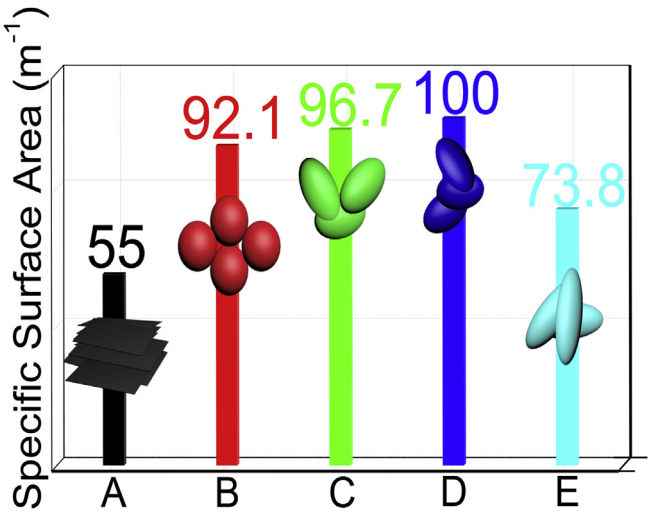

Fig. 6. Diagram of 2D, spherical and ellipsoidal materials at different ratios of polar radius (c) and equatorial radius (a); A: 2 D material, B: Ball (c: a = 1:1), C: Ellipsoid (c: a = 2:1), D: carbon of this work (c: a = 2.5:1) and E: Ellipsoid (c: a = 3:1).

from 0.5 A g^{-1} to 100 A g^{-1} in 6 M KOH electrolyte. In addition, the GCD curves present isosceles triangular shapes in the working voltage range from −0.9 to 0.1 V, indicating that the PC has typical capacitance properties during charge and discharge cycles. By increasing the current density from 1 A g^{-1} to 100 A g^{-1}, the charge time is greatly reduced from 610 s to 4.4 s, and 72.1% of 306.4 F g^{-1} is still remained under the ultrahigh current density, reflecting an excellent rate property of PC. The carbon offers significant high charge speed, and only 4.4 s is required for one process, which is suitable for potential applications in electric vehicles.

Fig. 5b displays CV curves of the obtained PC at different scan rates in 6 M KOH. The CV present approximately rectangular shapes without obvious redox peaks, indicating the typical charge/discharge process of double-layer capacitance. The current is raised very fast by increasing the scan rate, showing that the carbon has a rapid response ability.

Fig. 5c illustrates the rate performances of the obtained PC at different current densities. The as-prepared PC electrodes were charged/discharged at various current densities of 1, 2, 5, 10, 20, 50, 80 and 100 A g^{-1} for 100 cycles per step, totally 15 steps. The observed specific capacitances were found to be 303.8, 273.4, 257.6, 254.2, 244.1, 226.1, 198.5 and 190.4 F g^{-1}, respectively. It is important that when the current density is ultra-high, up to 100 A g^{-1}, the reversible capacitance still retains 190.4 F g^{-1}, which is circa 62.7% of that for 1 A g^{-1}, indicating an excellent rate performance. In particular, when the current density is decreased from 100 A g^{-1} to initial value of 1 A g^{-1}, the capacitance recovers to 299.2 F g^{-1}, which is approximately 98.5% of the initial value after 1500 cycles, exhibiting superior reversibility against cycling.

Recently, several research groups have reported some 3D PC and nitrogen-doped PC with high specific capacitance and long life [33,34,37–40,45–56]. The electrochemical properties of these materials and the as-prepared PCs are compared in Fig. 5d and Table S1. The PC synthesized in this work provides superior capacitance and excellent rate properties as compared with the reported materials, indicating that the obtained PC is an outstanding active material for SPs. The prepared PC has shown remarkable electrochemical properties at ultrahigh current density, which will be very useful in power sources of electric vehicles. These properties are attributed to its ellipsoidal structure and natural porous structure.

In order to prove that the ellipsoidal structure is beneficial to improving the electromhemical performance at high current density, we calculate the specific volume surface area versus different structures. Fig. 6 shows a schematic diagram of different structures of 2D materials such as: spherical and ellipsoid with different ratio of polar radius (c) and equatorial radius (a). The effective area of 2D materials decreases through an overlap of each other. For spherical or ellipsoid materials, their spherical or oval-shaped profiles will effectively minimize the loss of electrochemical reaction surface area. In general, the spherical material can be considered as special case of c: a = 1: 1. In addition, Fig. 6 displays the effective specific surface areas versus different c: a values. The largest specific surface area is obtained when the c: a value is 2.5: 1 on the basis of the same volume. The results of HR-TEM and SEM images show that the obtained PC material has a length of

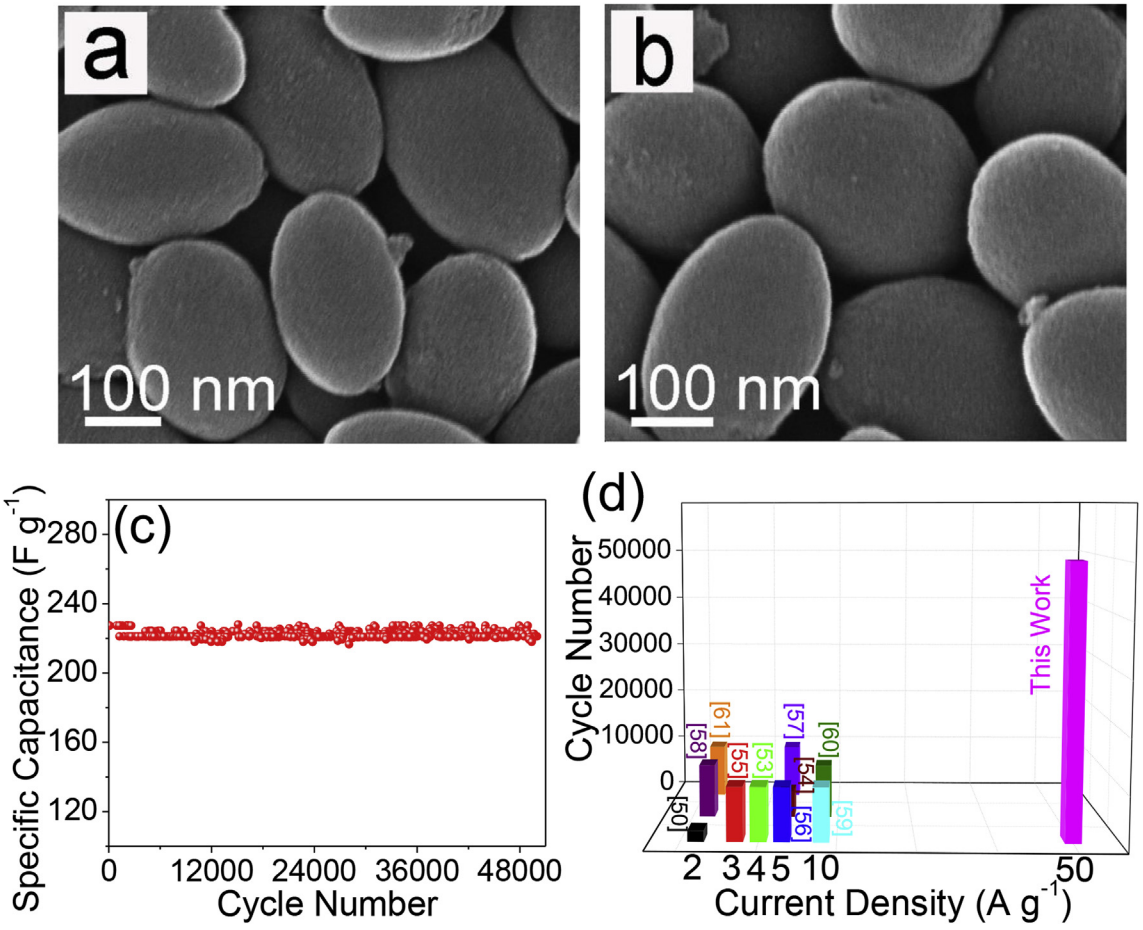

Fig. 7. SEM images of the obtained PC (a) before and (b) after 50,000 cycles, (c) SC curve of the obtained PC after the 50,000 charge and discharge cycles at 50 A g^{-1} in 6 M KOH and (d) the cycling life of the obtained PC and the other PC reported in literature.

900–1000 nm and a width of 350–400 nm, so its c: a value is close to its optical c: a value of 2.5. Therefore, due to this property, the obtained PC material have superior ultrahigh charge and discharge speed compared to other carbon materials reported in literature [50,53–61].

Fig. 7a and b shows SEM images of the obtained PC before and after 50,000 cycles. The PC structure in Fig. 7b almost keeps the initial morphology on its surface after 50,000 cycles compared to Fig. 7a. Fig. 7c shows the cycling stability of the PC for 50,000 cycles at the ultrahigh current density of 50 A g^{-1}. The obtained PC provides excellent durability with very slight decay of 5.05% after the 50,000 cycles, which is remarkably superior to the existing materials reported in literature [54–60]. Fig. 7d shows the cycling life of the PC and other carbons reported in literature [50,53–61]. It can be seen that the cycling number and capacitance retention ratio are much higher than those in the reported papers.

4. Conclusions

In conclusions, $Al(OH)_3$ and BTC are employed as raw materials to obtain Al-BTC and further produce C/Al_2O_3 by carbonation. PC is finally obtained by removing the Al_2O_3 from C/Al_2O_3 via the green approach. The beauty of the described methodology is that $Al(OH)_3$ can be recovered by the Bayer method for the next batch. The bonds of Al—O and carboxyl in Al-BTC are formed of natural pore agent. The specific surface area and pore volume of the rugby-like carbon are found to be 1400 $m^2 g^{-1}$ and 1.172 $cm^3 g^{-1}$, respectively. The PC offers excellent electrochemical performance due to its special structure (axis c/a ratio of 2.5). In addition, it has a specific capacitance up to 306.4 F g^{-1} at current density of 1 A g^{-1} and only 72.1% attenuation is observed when the current density increases from 1 A g^{-1} to 100 A g^{-1}. Furthermore, it has an excellent durability with only 5.05% decay after 50,000 cycles at current density of 50 A g^{-1}. Finally, it offers an ultrahigh charge speed, which can finish a charge process for only 4.4 s which is very suitable for potential application in electric vehicles.

Acknowledgements

This work was supported by the National Natural Science Foundation of China (21676022 & 21706004), and the Fundamental Research Funds for the Central Universities (BHYC1701A).

Appendix A. Supplementary data

Supplementary data to this article can be found online at https://doi.org/10.1016/j.jpowsour.2018.10.034.

References

[1] W. Li, F. Zhang, Y. Dou, Z. Wu, H. Liu, X. Qian, D. Gu, Y. Xia, B. Tu, D. Zhao, Adv. Energy Mater. 1 (2011) 382–386.
[2] Y. Zhang, S.J. Park, Carbon 122 (2017) 287–297.
[3] S. Guo, Y. Zhu, Y. Yan, Y. Min, J. Fan, Q. Xu, H. Yun, J. Power Sources 316 (2016) 176–182.
[4] T. Li, W. Zhang, L. Zhi, H. Yu, L. Dang, F. Shi, H. Xu, F. Hu, Z. Liu, Nano Energy 30 (2016) 9–17.
[5] L.F. Que, F.D. Yu, Z.B. Wang, D.M. Gu, Small 14 (2018) 1704508.
[6] W. Lu, M. Sevilla, A.B. Fuertes, M. Robert, Y. Gleb, Adv. Funct. Mater. 22 (2012) 827–834.
[7] C. Zheng, X. Zhou, H. Cao, G. Wang, Z. Liu, J. Power Sources 258 (2014) 290–296.
[8] Z. Yang, J. Zhang, M.C. Kintner–Meyer, X. Lu, D. Choi, J.P. Lemmon, J. Liu, Chem. Rev. 111 (2011) 3577–3613.

[9] S. Kondrat, C.R. Pérez, V. Presser, Y. Gogotsi, A.A. Kornyshev, Energy Environ. Sci. 5 (2012) 6474–6479.
[10] Q. Lu, Y. Chen, W. Li, J. Chen, J. Xiao, F. Jiao, J. Mater. Chem. 1 (2013) 2331–2336.
[11] L.F. Que, F.D. Yu, K.W. He, Z.B. Wang, D.M. Gu, Chem. Mater. 29 (2017) 9133–9141.
[12] L. Chen, T. Ji, L. Brisbin, J. Zhu, ACS Appl. Mater. Interfaces 7 (2015) 12230–12237.
[13] K. Wang, Y. Cao, X. Wang, Q. Fan, W. Gibbons, T. Johnson, B. Luo, Z. Gu, Energy 94 (2016) 666–671.
[14] L.F. Que, F. Yu, L. Zheng, Z. Wang, D. Gu, Nano Energy 45 (2018) 337–345.
[15] C. Choi, J.A. Lee, A.Y. Choi, Y.T. Kim, X. Lepro, M.D. Lima, R.H. Baughman, S.J. Kim, Adv. Mater. (Weinheim, Ger.) 26 (2014) 2059–2065.
[16] X. Fan, C. Yu, J. Yang, Z. Ling, C. Hu, M.D. Zhang, J. Qiu, Adv. Energy Mater. 5 (2015) 1401761.
[17] M. Sevilla, A.B. Fuertes, ACS Nano 8 (2014) 5069–5078.
[18] S.W. Zhang, B.S. Yin, C. Liu, Z.B. Wang, D.M. Gu, Chem. Eng. J. 349 (2018) 509–521.
[19] S. Yang, X. Feng, X. Wang, K. Müllen, Angew. Chem. Int. Ed. 50 (2011) 5339–5343.
[20] R. Menzel, S. Barg, M. Miranda, D.B. Anthony, S.M. Bawaked, M. Mokhtar, S.A. Al–Thabaiti, S.N. Basahel, E. Saiz, M.S.P. Shaffer, Adv. Funct. Mater. 25 (2015) 28–35.
[21] X. Yu, J. Zhao, R. Lv, Q. Liang, C. Zhan, Y. Bai, Z. Huang, W. Shen, F. Kang, J. Mater. Chem. 3 (2015) 18400–18405.
[22] D. Feng, T. Lei, M.R. Lukatskaya, J. Park, Z. Huang, M. Lee, L. Shaw, S. Chen, A.A. Yakovenko, A. Kulkarni, J. Xiao, K. Fredrickson, J.B. Tok, X. Zou, Y. Cui, Z. Bao, Nat. Energy. 3 (2018) 30–36.
[23] H.B. Wu, X.W. Lou, Sci. Adv. 3 (2017) eaap.9252.
[24] D. Dong, H. Guo, G. Li, L. Yan, X. Zhang, W. Song, Nano Energy 39 (2017) 470–477.
[25] D. Sheberla, J.C. Bachman, J.S. Elias, C. Sun, Y.S. Horn, M. Dinca, Nat. Mater. 16 (2017) 220–224.
[26] H. Sun, L. Mei, J. Liang, Z. Zhao, C. Lee, H. Fei, M. Ding, J. Lau, M. Li, C. Wang, X. Xu, G. Hao, B. Papandrea, I. Shakir, B. Dunn, Y. Huang, X. Duan, Science 356 (2017) 599–604.
[27] Y. Zhao, L. Goncharova, Q. Zhang, P. Kaghazchi, Q. Sun, A. Lushington, B. Wang, R. Li, X. Sun, Nano Lett. 17 (2017) 5653–5659.
[28] P. Zhang, B.Y. Guan, L. Yu, X.W. Lou, Angew. Chem. Int. Ed. 56 (2017) 7141–7145.
[29] N. Cheng, S. Stambula, D. Wang, M. Banis, J. Liu, A. Riese, B. Xiao, R. Li, T.-K. Sham, L. Liu, G. Botton, X. Sun, Nat. Commun. 7 (2016) 13638.
[30] K. Kaliyappan, J. Liu, B. Xiao, A. Lushington, R. Li, T.K. Sham, X. Sun, Adv. Funct. Mater. 27 (2017) 1701870.
[31] C. Qu, Y. Jiao, B. Zhao, D. Chen, R. Zou, K.S. Walton, M. Liu, Nano Energy 26 (2016) 66–73.
[32] S. Osman, R.A. Senthil, J. Pan, W. Li, J. Power Sources 391 (2018) 162–169.
[33] L. Xin, Q. Liu, J. Liu, R. Chen, R. Li, Z. Li, J. Wang, Electrochim. Acta 248 (2017) 215–224.
[34] X. Yan, X. Li, Z. Yan, Appl. Surf. Sci. 308 (2014) 306–310.
[35] Y. Chen, D. Ni, X. Yang, C. Liu, J. Yin, K. Cai, Electrochim. Acta 278 (2018) 114–123.
[36] S. Sundriyal, H. Kaur, S.K. Bhardwaj, S. Mishra, K.-H. Kim, A. Deep, Coord. Chem. Rev. 369 (2018) 15–38.
[37] J. Zhang, J. Xue, P. Li, S. Huang, H. Feng, H. Luo, Electrochim. Acta 284 (2018) 328–335.
[38] Y. Liu, J. Xu, S. Liu, Microporous Mesoporous Mater. 236 (2016) 94–99.
[39] Y. Yang, S. Hao, H. Zhao, Y. Wang, X. Zhang, Electrochim. Acta 180 (2015) 651–657.
[40] S. Zhang, X. Shi, D. Moszynski, T. Tang, P.K. Chu, X. Chen, E. Mijowska, Electrochim. Acta 269 (2018) 580–589.
[41] B. Xiao, B. Wang, J. Liu, K. Karthikeyan, Q. Sun, Y. Liu, G. Dadheech, M. Balogh, L. Yang, T.-K. Sham, R. Li, M. Cai, X. Sun, Nanomater. Energy 34 (2017) 120–130.
[42] R. Bendi, V. Kumar, V. Bhavanasi, K. Parida, P.S. Lee, Adv. Energy Mater. 6 (2016) 1501833.
[43] M. Yu, Li Zhang, X. He, H. Yu, J. Han, M. Wu, Mater. Lett. 172 (2016) 81–84.
[44] B. Gao, Y. Ma, J. Mei, S. Lu, L. Ren, Chem. Eng. J. 331 (2018) 597–605.
[45] N. Zhang, X. Yang, X. Yu, Y. Jia, J. Wang, L. Kong, Z. Jin, B. Sun, T. Luo, J. Liu, Chem. Eng. J. 252 (2014) 220–229.
[46] W. Bao, A.K. Mondal, J. Xu, C. Wang, D. Su, G. Wang, J. Power Sources 325 (2016) 286–291.
[47] J.A. Carrasco, J. Romero, G. Abellan, J. Hernandez-Saz, S.I. Molina, C. Marti-Gastaldo, E. Coronado, Chem. Commun. 52 (2016) 9141–9144.
[48] X. He, H. Zhang, H. Zhang, X. Li, N. Xiao, J. Qiu, J. Mater. Chem. 2 (2014) 19633.
[49] P. Zhang, F. Sun, Z. Shen, D. Cao, J. Mater. Chem. 2 (2014) 12873–12880.
[50] Y. Pan, Y. Zhao, S. Mu, Y. Wang, C. Jiang, Q. Liu, Q. Fang, M. Xue, S. Qiu, J. Mater. Chem. 5 (2017) 9544–9552.
[51] X. Chen, Y. He, H. Song, Z. Zhang, Carbon 72 (2014) 410–420.
[52] I.A. Khan, A. Badshah, I. Khan, D. Zhao, M.A. Nadeem, Microporous Mesoporous Mater. 253 (2017) 169–176.
[53] L. Wan, E. Shamsaei, C.D. Easton, D. Yu, Y. Liang, X. Chen, Z. Abbasi, A. Akbari, X. Zhang, H. Wang, Carbon 121 (2017) 330–336.
[54] J. Yang, G. Li, M. Cai, P. Pan, Z. Li, Y. Bao, Z. Chen, Chem. Commun. 53 (2017) 5028–5031.
[55] C. Wang, C. Liu, J. Li, X. Sun, J. Shen, W. Han, L. Wang, Chem. Commun. 53 (2017) 1751–1754.
[56] M. Karnan, K. Subramani, P.K. Srividhya, M. Sathish, Electrochim. Acta 228 (2017) 586–596.
[57] Y. Li, G. Wang, T. Wei, Z. Fan, P. Yan, Nano Energy 19 (2016) 165–175.
[58] K. Song, W. Song, L. Fan, J. Mater. Chem. 3 (2015) 16104–16111.
[59] L. Hu, X. Peng, Y. Lia, L. Wang, K. Huo, L.Y.S. Lee, K. Wong, P.K. Chub, Nano Energy 34 (2017) 515–523.
[60] Y. Liu, G. Li, Y. Guo, Y. Ying, X. Peng, ACS Appl. Mater. Interfaces 9 (2017) 14043–14050.
[61] L. Xin, Q. Liu, J. Liu, R. Chen, R.M. Li, Z. Li, J. Wang, Electrochim. Acta 248 (2017) 215–224.